

Numerical and experimental studies of the hypersonic flow around a cube at incidence

Thomas W. Rees^{a,*}, Paul J.K. Bruce^a, Tom B. Fisher^b, Mark K. Quinn^b, Jim A. Merrifield^c

^a Imperial College London, Exhibition Road, SW7 2AZ, London, United Kingdom

^b University of Manchester, Oxford Road, M13 9PL, Manchester, United Kingdom

^c Fluid Gravity Engineering Ltd., 1 West Street, PO10 7DX, Emsworth, United Kingdom



ARTICLE INFO

Keywords:
 Infrared thermography
 Heat transfer
 Inverse methods
 Hypersonic
 Satellite demise
 Incidence

ABSTRACT

In order to improve predictions of the on-ground casualty risk associated with the uncontrolled atmospheric re-entry of satellites from Low Earth Orbit, there is significant research interest in the development of engineering models of hypersonic heating rates to faceted shapes. A key part of developing such models is generating accurate datasets of the heat fluxes experienced by faceted shapes at various orientations in hypersonic flows. In this work, we use wind tunnel experiments and CFD simulations to study the hypersonic flow around a cuboid geometry at 5° incidence in a Mach 5 flow at Reynolds numbers of 79.5×10^3 , 109×10^3 and 148×10^3 . The wind tunnel data are obtained in the University of Manchester's High SuperSonic Tunnel and consist of schlieren images and temperature histories collected using infrared thermography. These temperature histories are used to calculate experimental heat fluxes by solving a three-dimensional inverse heat conduction problem. CFD simulations around the same geometry at equivalent free-stream conditions are calculated with the DLR-TAU code. The experimental and CFD results show good agreement both in terms of heat fluxes as well as flow structure. Notable flow structures include wedge-shaped regions of high heat flux which emanate from the windward corners of the cube. Analysis of numerical Q-criterion contours show that these high heat flux regions are caused by vortex structures generated by the expansion at the cube corner. Analysis of the numerical skin friction coefficient shows that even at incidence there is no breakaway separation from the expansion edges of the cube and the flow remains attached throughout. We show that although there is little change in the average heat flux experienced by a cube at 5° incidence to the free-stream compared to one at 0° incidence, there are significant changes in the heat flux contours over the cubes at these two incidences. Finally, we calculate a number of heating shape factors which can easily be implemented in satellite re-entry and demise prediction analysis tools.

1. Introduction

One of the important consequences of humanity's rapidly increasing usage of the near-Earth space environment is the increasing risk associated with space debris. The Kessler syndrome, first postulated in a 1978 paper by Kessler and Cour-Palais [1], is one of the most important dangers associated with space debris. This phenomenon could occur should the density of debris in Earth orbit become so great that collisions are inevitable. In this case, the generation of new debris from a collision would lead to a sequence of in-orbit collisions which would exponentially increase the amount of debris in orbit and would eventually render new space missions too hazardous to conduct until the quantity of debris is significantly reduced.

One way to mitigate the risk of a Kessler syndrome trigger is to properly dispose of satellites and other debris such as spent upper rocket stages at the end of their operational lifespan. Post mission disposal is one of the Inter-Agency Space Debris Coordination Committee's (IADC) guidelines for the mitigation of space debris [2]. For satellites in Geostationary Earth Orbit (GEO), their high altitudes mean the most cost-effective disposal method is to raise their orbits to a so-called 'graveyard orbit', which places them well away from other commonly used orbits. For satellites in Low Earth Orbit (LEO), such re-orbiting manoeuvres are far too expensive in terms of propellant use and the associated costs of increased satellite mass, and alternative disposal methods are necessary. This usually means de-orbiting the satellite so that it re-enters the Earth's atmosphere. For smaller satellites, the

* Corresponding author.

E-mail address: thomas.rees10@imperial.ac.uk (T.W. Rees).

extreme temperatures and forces experienced during a re-entry event will completely destroy the satellite, and any parts that impact the ground will have minimal energy. For larger debris however, it becomes more likely that significant quantities of satellite mass will impact the ground.

If the kinetic energies and cross sectional areas of the satellite debris impacting the ground are large enough, then the risk of ground casualties associated with the re-entry event is non-negligible. To mitigate this, NASA published safety standard 1740.14 in 1995 which first proposed an acceptable casualty risk of 1 in 10^4 per re-entry event [3]. This value has since become the consensus acceptable debris re-entry ground casualty risk [2]. In order to estimate the ground-casualty risks associated with re-entry events, specialized tools such as DRAMA (Debris Risk Assessment and Mitigation Analysis) [4], SCARAB (SpaceCraft Atmospheric Re-entry and Aerothermal Break-up) [5], and ORSAT (Object Re-entry Survival Analysis Tool) [6] have been developed. Although each of these tools has different strategies for treating the re-entry problem, they all broadly use the same work flow: model the aerothermodynamic heating and forces on each object during re-entry, use these heating rates and forces to calculate how the objects break up and then burn up, and then use knowledge of the effective cross-sections of the surviving components and a population density map of the Earth to estimate the casualty risk associated with each surviving component and therefore the entire re-entry event.

Obviously this is an extremely complicated simulation which has significant uncertainty attached to it. In particular, calculations of the aerothermodynamic heating rates induced by the hypersonic flow around the objects currently rely on correlations developed for simple rounded objects such as capsule-shaped spacecraft. These correlations are then extrapolated to be applied to complex satellite geometries, which are significantly different from the geometries these correlations were designed for. Satellite geometries are notably typified by sharp corners, facets, and other multi-scale structures. Such geometric features cause strong expansions or compressions of the flow around the body. These have a significant effect on local heat fluxes. Furthermore, these pressure gradients can even be strong enough to cause local separations which could further affect both the heat fluxes and aerodynamic forces experienced by the body.

The development of new heating correlations designed specifically for the faceted shapes typical of satellite geometries is hampered by the fact that there is a lack of freely available high-fidelity data, whether experimental or numerical, of heat fluxes to faceted shapes other than flat-ended cylinders (which have been extensively analysed both experimentally and theoretically in the 1960s [7–11]). Notable among previous studies of cylinders are the experimental studies of Matthews & Eaves [9] which identified that, at certain conditions, a separation bubble can form immediately downstream of a cylinder's sharp expansion corner. The authors suggested that the heat fluxes under the separation, and the formation of the separation itself, are both highly dependent on the Reynolds number. A recent 2D CFD study investigating the effect of Reynolds number on the hypersonic flow around faceted shapes confirmed that the formation of such a separation bubble was dependent on Reynolds number [12], and that the presence of a separation could significantly decrease local heat fluxes. However, none of these studies investigated the effect of incidence on these flow structures.

The heating rates to cuboids were first studied in the reports of Crosby & Knox [13], and Laganelli [14], who experimentally measured heat fluxes to a cube in a Mach 8 flow at discrete locations using thin-foil calorimeters. More recently, measurements of the hypersonic heat fluxes to a cube were made using InfraRed Thermography (IRT) [15] so that the heat fluxes across the entire surface of the cube could be measured, rather than just at discrete points on the geometry. These IRT measurements identified regions of increased heating along the streamwise edges of the cube, which were attributed to the presence of vortical structures emanating from the cube's sharp corners. Similar structures

had previously been identified in oil-flow visualization on rectangular cylinders protruding from flat plates [16], but their effect on heat fluxes had not yet been quantified. One issue with these previous studies of both cuboids and cylinders is that they all consider models at zero degrees incidence. In reality, satellites during re-entry will be randomly tumbling, constantly changing their attitude relative to the oncoming flow. Fortunately, the timescale of the tumbling motion is much longer than the characteristic timescale of the flow. As a result, analysis of tumbling can be simplified by considering the flow at every satellite attitude to be steady-state.

Numerical studies are an essential complement to experimental results as they can provide full flow-field data, including heat fluxes over the entire geometry including near edges and corners which are especially challenging to instrument in an experimental test. Numerical analyses are also faster and cheaper to perform than experiments, allowing researchers to quickly study more flow conditions and model orientations. There have been two recent notable efforts to build databases of CFD results of the hypersonic flow around faceted shapes. The French Space Agency, CNES has developed a significant database of approximately seventy 2D and 3D CFD simulations of the hypersonic flow around thick flat plates, cuboid geometries, and other simple faceted shapes such as hemispheres and annular rings generated with the CEDRE and MISTRAL CFD codes [17,18]. The database contains simulations at a wide range of angles of attack, flight conditions, and considers a significant range of object sizes but unfortunately is not public. However, some of the database results for hollow hemispheres and annular rings have been validated experimentally in hypersonic wind tunnels [18].

The second set of numerical studies were performed in the context of the European Space Agency's (ESA) AeroThermoDynamics for Design for Demise (ATD3) working group [19,20]. This working group gathered simulation results, generated by a range of industrial and academic partners, of the hypersonic flow around a range of faceted shapes, including cuboids, cylinders, hollow cylinders, and flat plates, but at a more limited range of flight conditions and incidences than the CNES database. Unfortunately, like the CNES database, the detailed results of these simulations have not been published, making it difficult to use them to generate new heating correlations. In addition to these two larger initiatives, other small numerical studies have been performed looking at more specific flow conditions such as super-orbital re-entry flows [21].

The scope of this paper is to expand on previous experimental studies of the hypersonic heating rates to a cube, which had all considered the flow around a cube at 0° incidence. Using both numerical and experimental methods, this work will investigate the effect of small angles of incidence on the hypersonic flow-field around a cuboid. The numerical simulations will provide a method to visualize the 'hot wedges' identified in Ref. [15] which significantly increase the heat fluxes to certain regions of the cube when it is at zero incidence, as well as a method to investigate the effect of incidence on these flow structures. The experimental flows will supplement the numerical results by providing valuable validation data. These experimental flows will be visualized with schlieren photography, and the heat fluxes will be calculated by applying a 3D inverse heat conduction problem (IHCP) to IRT temperature data [15]. Finally, we aim to use the combined experimental and numerical datasets to draw conclusions about the effect of small angles of incidence on the hypersonic heat fluxes to faceted shapes. We will place special emphasis on generating correlations and drawing conclusions that are useful and impactful in the context of the development of new simple heating models for satellite re-entry tools. This paper starts with a description of the CFD code and meshing tools used for the numerical simulations before describing the facilities, measurement techniques, and data postprocessing algorithms used to acquire the experimental data. This is followed by a presentation of the results, a discussion of their key consequences, and finally our conclusions.

2. Numerical simulations

2.1. Flow solver and models

The numerical simulations of the flow are performed using the DLR-TAU CFD code, which has a history of successful usage and validation for simulations of hypersonic flows [19,22–24]. TAU solves the three-dimensional compressible Navier-Stokes equations using a finite volume method on a hybrid unstructured mesh. The mesh can be built with prisms, tetrahedra, and hexahedra. The code includes a number of turbulence models depending on user requirements. This includes boundary-layer transition models. In addition to turbulence models, TAU includes a number of chemical reaction and thermal non-equilibrium models. The user also has a wide choice of different flux discretization and time discretization methods, including both first and second order accurate methods. Further advanced models such as Large Eddy Simulation (LES) have also been incorporated into the code. In addition to the comprehensive range of physics models, the code also includes a powerful grid adaptation module which can refine the mesh using a number of user-defined rules. Due to the relatively low Reynolds numbers and enthalpies tested in the wind tunnel experiments, the current simulations solve the non-reacting compressible laminar Navier-Stokes equations. The flux discretization method used is the Advection Upstream Splitting Method – Difference Vector splitting biased (AUSMDV) scheme, with second order accuracy in space [25]. The simulations are assumed to be steady in time, with a backwards-Euler scheme providing the time integration.

2.2. Geometry, boundary conditions, and mesh

The geometry considered is the same across all the simulated flow conditions. The geometry is a cuboid with dimensions $0.03 \times 0.03 \times 0.04$ m in a quasi-hemispherical domain with radius 0.075 m. The back face (and therefore wake) are not included in the simulation. The inclusion of these regions of complex flow would significantly increase the complexity of the modelling required to achieve an accurate and converged solution. Furthermore, the heat fluxes on the back surface are likely to be negligible compared to the heating to the rest of the cube. In order to improve the numerical stability of the simulations, the edges and corners of the cube have a fillet of radius 1×10^{-4} m applied to them. The cube surface boundary condition is a non-slip isothermal wall condition with uniform $T_w = 300$ K. An important point to emphasize here is that such a boundary condition is non-physical and not representative of a true re-entry flow. In reality, the flow is transient rather than steady state due to the increase of the wall temperature (approaching the adiabatic wall temperature). Furthermore, this temperature increase will not be uniform across the geometry – due to the increased heat flux expected at the edges, corners, and the stagnation surface of the cube, these regions will warm up much more quickly than other areas of the cube geometry. Normally, this effect can be mitigated by presenting the heat flux results as Stanton numbers. However, the Stanton number normalization cannot take into account the fact that there will likely be thermal conduction through the geometry near corners and edges, and therefore the CFD results in these regions may not be representative of reality. Unfortunately, the only way to capture this physical phenomenon is to run an unsteady CFD simulation which is fully coupled to a material thermal response simulation. In this case, the heat flux calculated by the CFD solver is fed into the material thermal solver, which then in turn supplies the wall temperature for the next time step in the CFD solver. Such a complex simulation is beyond the scope of this work, and we will instead interpret the current CFD simulations with this limitation in mind.

For all flow cases considered, the initial mesh was generated using CENTAUR, a hybrid meshing software which generates meshes of prism cells near viscous boundaries and tetrahedral cells elsewhere. Unusually,

for a symmetric shape such as a cube, the entire cube geometry was meshed and simulated, instead of meshing a half-cube with symmetry boundary conditions. This was done because simulations with a half-cube geometry showed non-physical heat flux profiles on the stagnation surface of the cube – the cause of this is unknown. As the CFD simulation converged, this initial mesh was adapted using TAU's mesh adaptation module, adding 30% more points to the mesh in each adaptation loop. Mesh convergence was achieved after 5 mesh adaptations, at which point the difference between the total heat flow to the cube (the surface integral of the heat flux to the cube) between mesh adaptation cycles was $< 0.5\%$. A slice through the final mesh is shown in Fig. 1. The final mesh size was approximately 40×10^6 points. In order to assure mesh independence of the heat flux results, the boundary-layer prism mesh generated by CENTAUR was specified to have a first cell height of 5×10^{-7} m, a mesh growth rate away from the wall of 1.2, and a total height of 24 cells. As a result, the first cell Reynolds number Re_c , defined as

$$Re_c = \frac{\rho_c a_c \Delta x}{\mu_c} \quad (1)$$

where ρ_c , a_c , and μ_c are the density, speed of sound, and viscosity of the fluid in the cell, and Δx is the characteristic length scale of the cell (usually the longest spatial dimension), never increases beyond 1 throughout the mesh for all flow conditions. The first cell Reynolds number is a commonly used condition to assure accurate resolution of surface heat flux by ensuring that flow gradients in the viscous boundary-layer region near the wall are accurately resolved [26,27].

2.3. Flow conditions and convergence criteria

The simulated inlet flow conditions shown in Table 1 are selected to match the experimental flow conditions described in Table 3. At this point we stress the orientation of the cube: the incidence angle of the cube is in the plane of the diagonal of the cube (see Section 3.1.2 and Figs. 4 and 3a for reference). The reason for this choice of cube orientation is largely driven by the practicalities of the experimental tests. This is described in more detail in Sections 3.1.2 and 3.2.1. In order to assess convergence of the simulations, two conditions are used: the

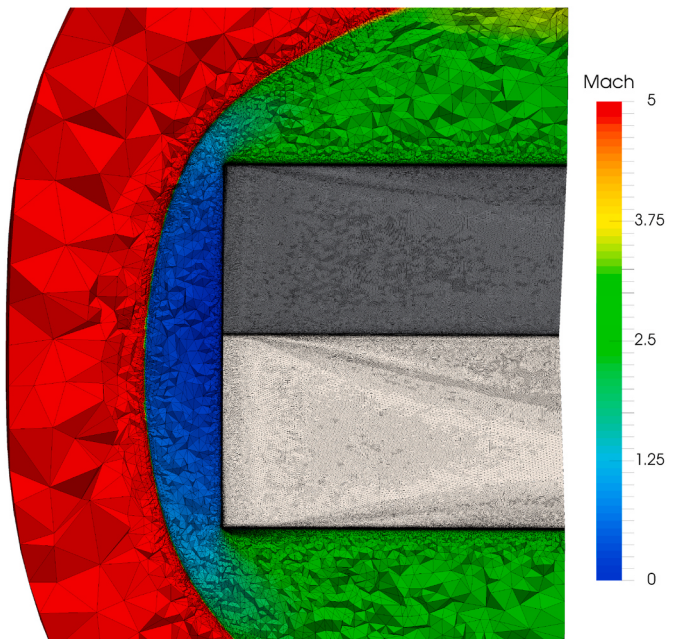


Fig. 1. Slice along the centreline of the final 3D mesh used for simulations at flow condition 3.

Table 1

Numerical flow conditions. Reynolds numbers are calculated using the cube length $L = 30$ mm.

Case No.	M	$Re \times 10^3$	u_∞	ρ_∞	T_∞	Angle of Attack
	[–]	[–]	[m/s]	[kg/m ³]	[K]	[°]
1 Num	5.0	79.5	1155	0.0210	132.7	5
2 Num	5.0	109	1180	0.0295	138.5	5
3 Num	5.0	148	1180	0.0400	138.0	5

reduction in the RMS density residual, and the total heat flow to the cube. Convergence was judged to have been achieved when the normalized RMS density residual either dropped below 10^{-6} or stopped reducing, and the change in total heat flow between iterations was less than 0.1%.

3. Experimental heat flux measurements

3.1. Experimental flow facility, models, and test conditions

3.1.1. High Supersonic Tunnel

The experiments were conducted in the University of Manchester's High Supersonic Tunnel (HSST), a long-duration blow-down facility. At Mach 5 it can achieve a stable test time of approximately 7 s with total pressures up to 850 kPa and, through the use of an electric resistive heater, total temperatures of up to 950 K. The nozzle has a 6 inch diameter outlet which exhausts to an evacuated working section. The working section has optical access via two parallel rectangular quartz windows which span the full useful length of the test jet. Schlieren images are acquired through Töpler's Z-type schlieren method. Two 12 inch diameter f/7.9 mirrors pass the light from a Newport optics model 66921 Xenon arc lamp, typically at 450 W, onto the knife-edge in the cut-off plane which is then focused through a 500 mm focal length achromatic doublet lens onto the camera sensor. The images are captured with a commercial Nikon D5200 24-megapixel DSLR camera. Infrared access is enabled by a 75 mm diameter uncoated germanium window mounted to the test section ceiling. Models can be mounted either on rails on the floor of the tunnel, or via the use of an arc-balance sting. The sting allows models to be mounted at angles of attack between $\pm 20^\circ$. Model orientation on the sting is fixed by a keyway and a number of grub-screws. A schematic diagram of the tunnel is presented in Fig. 2, and a table of the achievable flow conditions with a Mach 5 nozzle are presented in Table 2. A detailed description of the tunnel and its operation can be found in Refs. [28,29].

3.1.2. Model, mounting, and orientation

The model geometry is a 30 mm length cube, which is fitted to a 10 mm long additively-manufactured adaptor which is used to mount

the model to the sting interface. By swapping the sting adaptor, models can be mounted in different roll orientations, allowing different facets of the cube to be imaged by the IR camera and schlieren apparatus. For IRT measurements, the cube model is oriented in a rolled 45° orientation such that three surfaces of the cube are imaged simultaneously (see Fig. 4 for a sample IR image of a cube model). In this way, temperature data at a 3D corner of the cube can be obtained. As a result of mounting the cube in this particular orientation, the incidence angle of the cube is in the direction of the diagonal of the cube. A schematic diagram and photograph of the model in the wind tunnel working section is presented in Fig. 3.

The models are manufactured from MACOR®, a machinable glass-ceramic. MACOR was chosen due to its low diffusivity, high emissivity, success in previous experimental hypersonic IRT applications [15, 30], and ease of machining. Measurements of the temperature variation of MACOR's thermal properties are known from Refs. [15,31]. The directional emissivity variation of MACOR has been reported in Ref. [30]. Imbriale [31] correlated this data to find a correlation of the form

$$\varepsilon(\theta) = (\varepsilon_0 \cos(\theta))^{\frac{a}{\cos^b(\theta)}}, \quad (2)$$

with coefficients $\varepsilon_0 = 0.934$, $a = 0.0098$, and $b = 2.4$. The temperature variation of the emissivity of MACOR is unknown, and is assumed to be negligible in the current tests. However, measurements of the emissivity temperature variation of ceramic materials such as fused silica glass [32] suggest that the emissivity variation of such materials is very small up to temperatures of the order of 530 K. For the current experiments, the model temperatures can get much higher than this at the edges and corners of the model, where heat fluxes are highest (up to 700 K at the windward corner). This uncertainty in emissivity is partially taken into account in our error analysis (Section 3.3). However the uncertain nature of the emissivity variation of MACOR adds additional uncertainty at the corners and edges.

The sting adaptors are manufactured from Rigur™, a 3D printed simulated polypropylene with a high thermal deformation temperature [33].

3.1.3. Test conditions

In order to allow a direct comparison between the heat fluxes experienced by the cube at 0° and 5° incidence, the experimental test conditions are chosen to match the test conditions reported in Ref. [15]. These conditions in turn were specifically chosen in order to investigate the effect of Reynolds number variation on the flow field while maintaining a constant Mach number. While the flow is less energetic than real re-entry flows, the Reynolds numbers tested are still representative of re-entry Reynolds numbers, which are typically on the order of 10^4 at an altitude of 80 km. Furthermore, due to the exponential increase in the density of the Earth's atmosphere during the initial stages of re-entry,

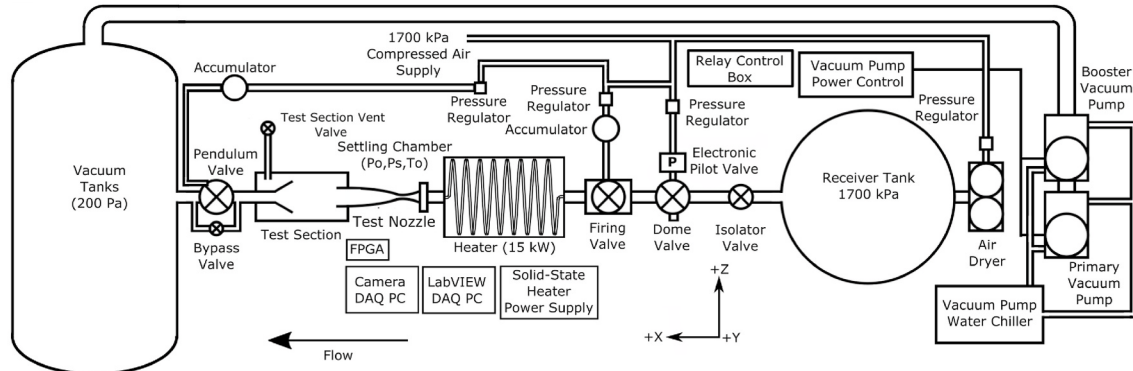
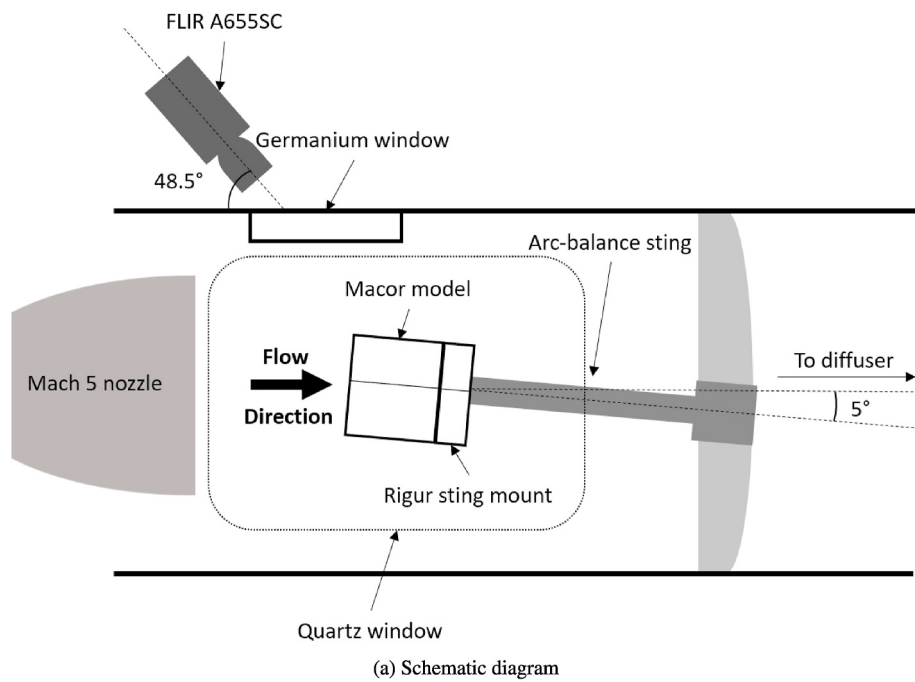
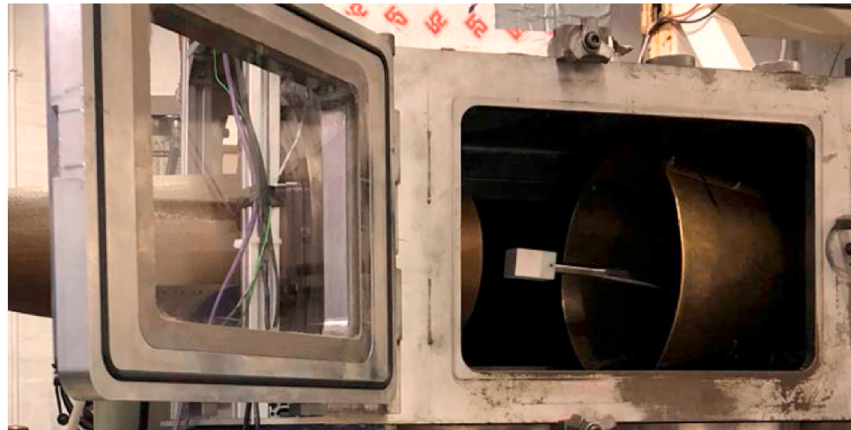


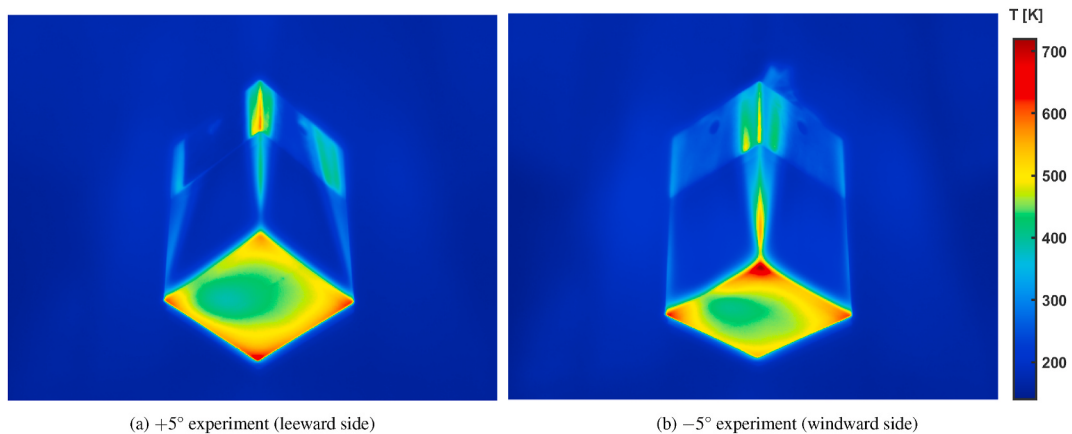
Fig. 2. Schematic diagram of the HSST facility.



(a) Schematic diagram



(b) Photograph

Fig. 3. Experimental set-up in the HSST working section.

(a) +5° experiment (leeward side)

(b) -5° experiment (windward side)

Fig. 4. IRT temperature contours at $t = 6$ s for the $Re = 148 \times 10^3$ tests.

Table 2
HSST characteristic flow conditions with a Mach 5 nozzle.

Parameter	Min	Max
T_0 range [K]	320	950
P_0 range [kPa]	200	850
run time [s]	0.5	7.5
Enthalpy [kJ/kg]	19.8	654
$Re \times 10^5$ [m ⁻¹]	9.69	226
Test jet diameter [m]	0.152	
Test gas	Air	

the Reynolds number of re-entry flows varies rapidly at altitudes around 80 km while the Mach number only varies weakly. Because of this, as well as the fact that hypersonic flows are generally only weakly dependent on Mach number (known as Mach number independence), we are confident that these experimental conditions can still provide valuable insight into re-entry flow behaviour.

Unfortunately not every flow condition in Ref. [15] was able to be matched. By mounting the model in the wind tunnel at incidence, the blockage area was increased, preventing the tunnel from starting at the lowest total pressure conditions tests in Ref. [15]. For each free-stream flow condition, two experiments are performed: one with the cube at +5° incidence, and one with -5° incidence. This is necessary due to the fact that only one IR camera is used and so IR data can only be captured for one half of the cube. A full description of the experimental conditions and tests is presented in Table 3.

3.2. InfraRed measurements and heat flux calculation

3.2.1. InfraRed camera and image processing

The infrared camera used is a FLIR A655SC fitted with a 25° FOV lens. The detector resolution is 640 × 480 pixels, and the frame rate is 50 Hz. It is mounted to a Minitec frame fixed to the floor of the laboratory to prevent any vibration transmission from the wind tunnel. The camera is positioned at a 48.5° angle to the horizontal axis of the model (Fig. 3), which allows it to image three sides of the cube model, as discussed in Section 3.1.2. The camera is calibrated using a Fluke 9132 portable infrared calibrator. The calibrator consists of a quasi-blackbody target with $\epsilon = 0.95$ which can be heated up to 500°C in 0.1°C increments. The calibration equation, which can be obtained by following the derivations described in Refs. [15,34], is

$$I_D = \epsilon \frac{R}{e^{B/T_{obj}} - F} + (1 - \epsilon) \frac{R}{e^{B/T_{amb}} - F} + C, \quad (3)$$

where R , B , F , and C are the calibration constants to be found, I_D is the radiant intensity, ϵ is the calibration target emissivity, T_{obj} is the calibration target temperature, and T_{amb} is the ambient temperature. The additional constant C is added to the usual Planck calibration equation used for IRT in order to take into account the IR emission of the germanium window [15]. The addition of such a constant was first proposed by Zaccarra et al. [35] as a way of taking the camera

Non-Uniformity Correction (NUC) into account and to regulate the different gains and zero offsets of each pixel in the Focal Plane Array. In the present case, it simply represents and corrects for window emission. The camera NUC is taken into account by calibrating the camera to a NUC-corrected intensity value I_{Dc} , called the Object Signal. The Object Signal is directly proportional to I_D and is calculated by the camera's firmware.

The calibration is performed in-situ, that is with the calibrator placed in the tunnel working section with the camera viewing the calibrator through the germanium window. For this reason, the effect of the window transmissivity is captured in the calibration coefficients R and C and does not need to be explicitly accounted for in the calibration equation [34]. During the calibration, the signal of the calibration target is recorded at 55 evenly spaced data points between 293.6 K and 676.5 K. The Levenberg-Marquardt nonlinear least squares algorithm is used to calculate the calibration coefficients R , B , F , and C in Eqn. (3). The final calibration curve has a coefficient of determination $R^2 = 0.997$ and an RMS error $\sigma = 0.1$ K.

3.2.2. Image processing

Once the raw IR data has been acquired by the camera (Fig. 4), it must be transformed to temperature values organized in a data structure suitable for input to the heat flux calculation method. This section provides a summary of the process; a more detailed description of the process can be found in Ref. [15]. Following the data collection, the raw data is filtered using a three-dimensional Savitsky-Golay filter in both space and time [36,37]. Following filtering, the IR video is stabilized using the single-step discrete Fourier transform approach to image registration proposed by Guizar-Sicairos et al. [38].

In order to transform the stabilized IR video into inputs suitable for the heat flux calculation method, the different surfaces of the cube in the IR image must be identified, and then an affine transformation be calculated in order to transform the perspective view of each of the cube faces in the raw image to square arrays of temperature. This is achieved by identifying the outer edges of the cube in the IR image with a fuzzy-logic-based edge detection algorithm. The inner edges of the cube cannot be identified using a conventional edge-detection algorithm as they do not necessarily correspond to regions of increased intensity gradient. Instead, these edges are assumed to be located at the location of maximum temperature. These assumptions regarding the edge location are not straightforwardly justifiable, and their effect on the experimental error associated with the heat flux measurements is discussed in Section 3.3.

Once the most likely locations of the cube edges are extracted their intersections are used to define the corners of the cube. These corner locations are used to define the moving points of an affine transformation to a square. During the calculation of the affine transformation, the IR image is down-sampled to give a final spatial resolution of the cube temperature maps of 2 pix/mm. Once the transformation has been calculated for every image frame, the temperature map for each surface of the cube is calculated by applying the infrared calibration (Eqn. (3)) separately to each surface. By applying the calibration independently to each surface, the variation in emissivity of each surface (due to the directional emissivity effect) can be taken into account. In order to calculate the directional emissivity for each cube face, the viewing angle θ to each surface is calculated using knowledge of the camera viewing direction \mathbf{W} (this is known from the camera's orientation in its mounting position), and normal vector to each of the cube's faces \mathbf{n} (which is known from the cube's orientation on the sting):

$$\theta = \arccos \left| \frac{\mathbf{W} \cdot \mathbf{n}}{|\mathbf{W}|} \right|. \quad (4)$$

3.2.3. Heat flux calculation by the solution of an inverse heat conduction problem

Once the temperature history of the cube has been measured using

Table 3
Experimental flow conditions. Reynolds numbers are calculated using the cube length $L = 30$ mm. and incidence angles are in the plane of the cube's diagonal.

Case No.	M	$Re \times 10^3$	ρ_∞	T_∞	Incidence angle
	[–]	[–]	[ρ_∞]	[K]	[–]
1 Exp+	5	79.5	0.0210	132.7	+ 5°
1 Exp-	5	79.5	0.0210	132.7	- 5°
2 Exp+	5	109	0.0295	138.5	+ 5°
2 Exp-	5	109	0.0295	138.5	- 5°
3 Exp+	5	148	0.0400	138.0	+ 5°
3 Exp-	5	148	0.0400	138.0	- 5°

IRT, the heat flux to the surface can be calculated by the solution of the heat conduction equation in the region of temperature measurement. For the present experiments ‘the region of temperature measurement’ essentially refers to the entire cube. For this work, this calculation is performed by solving an Inverse Heat Conduction Problem (IHCP). As opposed to solving the heat conduction equation directly using the temperature history as Dirichlet boundary conditions, the solution of the IHCP involves estimating the heat flux to the surface by the solution of an optimization problem. For a given heat flux, a numerically computed temperature profile is compared to the experimental temperature profile. The heat flux is then adjusted by the optimization procedure until the error between the computed and experimental heat flux histories is minimized. In order to perform this calculation, it is necessary to represent the test geometry with a numerical mesh. Due to the simple cuboid geometry considered in the current experiments, we use a simple equally spaced mesh with 2 pix/mm, corresponding to the down-sampled resolution of the IRT temperature results discussed above.

Although there are many different ways of solving an IHCP, in this work we use the Conjugate Gradient Method (CGM) [39] to minimize the following cost functional:

$$f(q(S, t)) = \int_0^{t_f} \sum_m^M m = 1(T_m(q(S, t)) - Y_m)^2 dt \quad (5)$$

where T_m is the computed temperature, Y_m is the measured temperature, t_f is the test time, and M is the total number of measurement locations (in this case, each point of the surface of the computational mesh, which also corresponds to each pixel of the transformed IR image frame as described in Section 3.2.1). A complete derivation and discussion of the equations (direct, adjoint, and sensitivity) solved during each iteration of the CGM can be found in Refs. [15,39,40]. In summary, at each iteration n of the optimization process, the following steps are performed:

1. Solve the direct heat equation with the latest heat flux estimate q_n as the boundary conditions.
2. Check the stopping criterion (Equation (6)). If satisfied, exit the iteration.
3. Solve the sensitivity problem, the solution of which gives the step size β_n in the conjugate direction of descent.
4. Solve the adjoint problem, the solution of which gives the conjugate direction of descent p_n of the system.
5. Update the solution where $q_{n+1} = q_n + \beta_n p_n$.

The stopping criterion of the CGM can be defined either by using a tolerance criterion, or by stopping when the algorithm reaches a minimum, that is, when there is negligible change in the cost functional after a direction re-set

$$f_n < \varepsilon, \quad (6)$$

where ε is some small value. In practice, the temperature measurement error will place a constraint on how small f_n can become. Following [39, 40], the temperature measurement residuals will be approximately equal to the standard deviation of the temperature measurement errors, that is:

$$T_m - Y_m \approx \sigma. \quad (7)$$

Therefore, ε in Eqn. (6) can be expressed by:

$$\varepsilon = M\sigma^2 t_f, \quad (8)$$

which gives the appropriate value of ε for the current problem.

For this work, the CGM algorithm has been implemented in Matlab. The direct, sensitivity, and adjoint problems are solved with the same forward-time central-space (FTCS) finite differencing scheme on an equally spaced, structured grid with $dx = 0.5$ mm. The IHCP is only

solved over one quarter of the cube – the quarter at the centre of the images presented in Fig. 4, giving a final grid size of 54×10^3 points. The boundary conditions at the three surfaces of the domain where temperatures are unknown are considered to be adiabatic. This is justified as the transverse conduction normal to the boundaries in these regions is likely to be small.

Once the conductive heat flux q has been evaluated, the modified Stanton number C_H is calculated, defined as:

$$C_H = \frac{q + q_{rad}}{\rho_\infty u_\infty (H_0 - h_w)} = \frac{q_{conv}}{\rho_\infty u_\infty (H_0 - h_w)}, \quad (9)$$

where q_{rad} is the total radiative heat flux away from a surface (given by the Stefan-Boltzmann equation) q_{conv} is the convective heat flux to the surface, and H_0 is the total enthalpy of the free-stream flow, given by:

$$H_0 = h_\infty + u_\infty^2 / 2. \quad (10)$$

In the remainder of this work, any reference to Stanton number refers to the modified Stanton number as defined above. The wall and free-stream enthalpy values h_w and h_∞ are calculated using the HOT thermal database package for Matlab and Octave [41].

3.3. Experimental error analysis

A comprehensive error analysis of the experimental set-up and heat flux calculation used in this work was performed in Ref. [15]. It indicated that the global error in the Stanton number values was within 12%. This global error value represented a spatially averaged error. On a local scale, errors were found to be higher near the edges and corners of the model (i.e. the regions where transverse conduction is most important), where the error values could reach up to 15%. By the same token, the error values in the cube regions away from the edges and corners were on the order of 9%. The analysis in Ref. [15] considered both the uncertainty inherent to the IHCP solution, as well as the sensitivity of the solution methodology to errors in the input data.

In addition to measurement errors, additional experimental error enters the solution through errors in the IRT image processing algorithm, and more specifically the edge detection methodology. Obviously, accurate identification of the cube location in the infrared image is a crucial aspect of obtaining accurate heat fluxes using the 3D-IHCP solution. As discussed in Section 3.2.2, edge detection algorithms generally rely on the assumption that edges are locations of high gradient (even if they may not place the edge at the region of highest gradient). This assumption is incorrect in the case of the inner edges of the cube in Fig. 4. The sensitivity of the 3D-IHCP solution to errors in the assumed edge locations of the cube was investigated in Ref. [15]. The results showed an extremely strong sensitivity. For the test cases considered in Ref. [15], it was found that the 3D-IHCP solution could show the presence of a region of non-physical negative Stanton number if edge location was wrong by 2 pixels (1 mm). As a consequence of this sensitivity, the Stanton number values near the edges will have a larger error associated with them.

4. Results

4.1. Surface heat flux

The modified Stanton numbers obtained from the TAU simulations and the 3D-IHCP solutions are presented in Figs. 5–7. In these figures, the contours are presented as if the cube has been ‘unfolded’ on to a flat surface. Due to the spatial symmetry of the flow, only results from 3 surfaces of the cube are presented. The spatial coordinates for these ‘unfolded’ cube plots, s and z are normalized by the experimental cube size $L = 0.03$ m. The experimental Stanton number values are calculated by time-averaging the Stanton number during 4 s of steady-state flow, as determined by the free-stream conditions (this corresponds to $2 < t < 6$

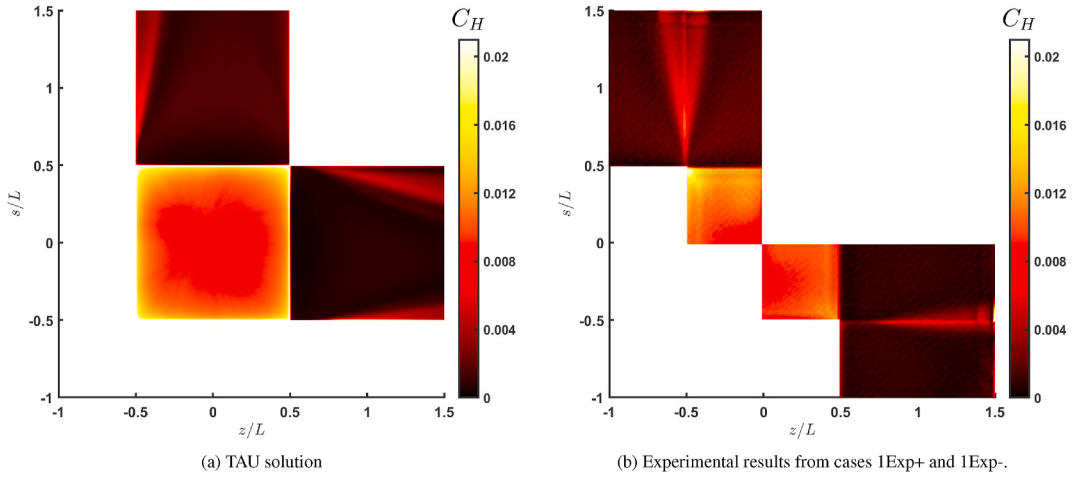


Fig. 5. Numerical and Experimental Stanton number contours for a cube at 5° incidence, in a Mach 5 flow with $Re = 79.5 \times 10^3$.

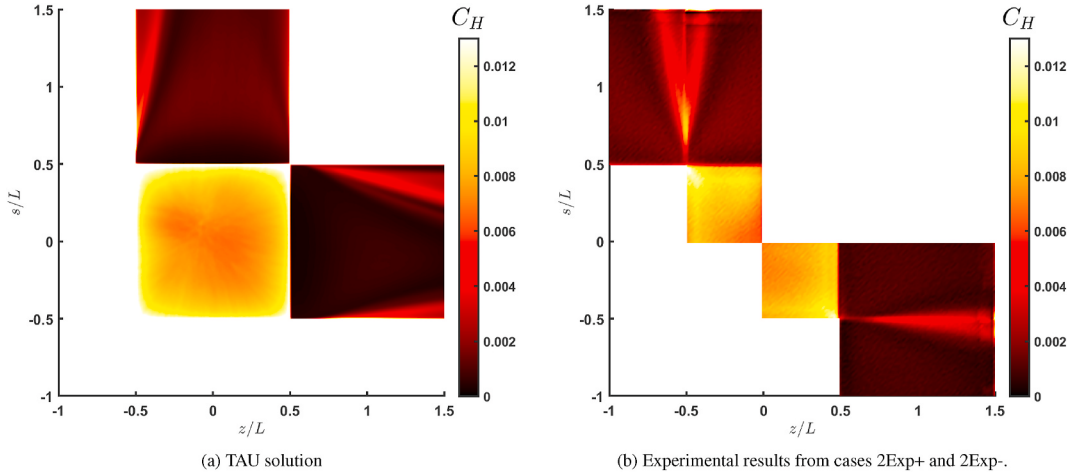


Fig. 6. Numerical and Experimental Stanton number contours for a cube at 5° incidence, in a Mach 5 flow with $Re = 109 \times 10^3$.

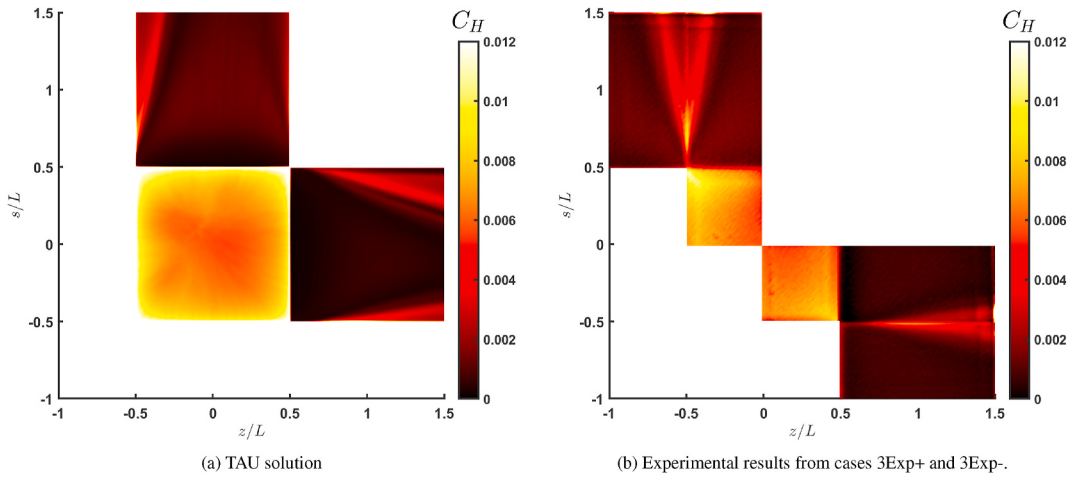


Fig. 7. Numerical and Experimental Stanton number contours for a cube at 5° incidence, in a Mach 5 flow with $Re = 148 \times 10^3$.

seconds of the tunnel run time). Furthermore, for each flow condition, the contours of experimental Stanton number (that is Figs. 5b, 6b and 7b) combine results from both experiments: one at positive and the other at negative incidence. Due to the viewing angle of the IR camera, it was only possible to calculate the heat fluxes along the $s/L = -0.5$ and $z/L = -0.5$ edges of the cube. These correspond to the edges at the centre of the images in Fig. 4. It is not possible to calculate heat fluxes along the $s/L = 0.5$ and $z/L = 0.5$ edges because the temperature histories which serve as the constraints for the 3D-IHCP could not be obtained on both sides of these edges. In principle, the data from both experiments could

$L = -0.5$ edges of the cube. These correspond to the edges at the centre of the images in Fig. 4. It is not possible to calculate heat fluxes along the $s/L = 0.5$ and $z/L = 0.5$ edges because the temperature histories which serve as the constraints for the 3D-IHCP could not be obtained on both sides of these edges. In principle, the data from both experiments could

be combined to obtain a temperature history for the entire cube, with which the 3D-IHCP could be solved over the entire cube. In practice this was not possible with the quality of data collected in these experiments.

We also introduce a distinction between the ‘windward’ and ‘leeward’ halves of the cube. The windward half refers to the two side faces of the cube most exposed to the free-stream flow. In the experiments, this is the half imaged by the IR camera during the -5° incidence tests (as seen in Fig. 4b and corresponding to the top half of the cube seen in Fig. 11a). The leeward side therefore refers the faces of the cube imaged by the IR camera during the $+5^\circ$ experiments (that is Fig. 4a and the top half of the cube in Fig. 11b). In Figs. 5–7, the windward side of the cube refers to the area of the plot above the diagonal line $s/L = z/L$, and the leeward side the area below the line.

In order to provide a direct comparison between the experimental and numerical results, Figs. 8 and 9 show plots of Stanton number for various constant values of s/L and z/L . Fig. 8 shows comparisons of Stanton number along the streamwise directions on the geometrical centreline of the cube, while Fig. 9 shows the Stanton number in the spanwise direction on the side faces of the cube. We stress again that the experimental results presented for each Reynolds number condition in these plots are combinations of results from two different experiments.

The trends in the C_H contours generally follow the expectation that the heat flux increases as the edges and corners of the cube are approached. This effect is more pronounced in the CFD simulations, where the heat flux at the windward edges of the cube appears to show an almost discontinuous spike which is not present in the experimental results. The results also show wedge-shaped regions of increased heat flux along the streamwise edges of the cube. These were previously identified in Ref. [15], which considered cubes at 0° incidence, and where the wedges were symmetrical along all four streamwise edges of the cube. In that study, these regions of increased heat flux were attributed to vortical structures being generated by the strong 3-dimensional expansion around the corners of the cube. However, it was not possible to verify that hypothesis solely using the experimental data collected in that study. In contrast to the symmetry of the flow around a cube at 0° incidence, the addition of a slight incidence to the cube creates a wider wedge spreading angle at the edge of the cube at $z/L = -0.5$ (on the center of the windward side of the cube), and a smaller spreading angle at $s/L = -0.5$ (on the center of the leeward side of the cube). The edge at $s/L = z/L = 0.5$ (which is the edge separating the windward and leeward surfaces of the cube) shows more complex behaviour: on the leeward surface of the cube ($z/L = 0.5$) there is a much wider spreading angle, while the windward surface of the cube ($s/L = 0.5$) shows no region of increased heating. Although no experimental heat flux results are available along the $s/L = 0.5$ and $z/L = 0.5$ edges, the presence of the much wider wedge spreading angles can be

confirmed by considering the raw IR temperature images (Fig. 4), where the effect of the increased heat flux can be observed as regions of increased temperature.

The direct comparisons of experimental and numerical results in Figs. 8 and 9 show relatively good agreement. As expected, Fig. 8 shows that the Stanton number along the stagnation surface of the cube (that is $-0.5 < s/L < 0.5$ in Fig. 8a and $-0.5 < z/L < 0.5$ in Fig. 8b) decreases as Reynolds number is increased. The experimental results appear to show significant noise in this region, leading to deviations from the CFD Stanton number values, especially for $0 < s/L < 0.5$ in Fig. 8a and $0 < z/L < 0.5$ in Fig. 8b. Finally, we note that the experimental results show consistently higher Stanton numbers immediately downstream of the expansion edges of the cube: for $0.5 < s/L < 1$ in Fig. 8a and $0.5 < z/L < 1$ in Fig. 8b.

4.2. Flow structures: schlieren images, Mach contours, and vortex visualization

In order to further investigate the flow-field and to confirm that the wedge shaped regions of higher heat flux are caused by vortices as hypothesized in Ref. [15], Fig. 10 shows isosurfaces of normalized Q-Criterion around the cube, coloured by Mach number. The Q-criterion [42] is a widely used definition of a vortex; a vortex is said to exist if

$$Q > \frac{1}{2} [\text{tr}(\nabla \mathbf{u})^2 - \text{tr}(\nabla \mathbf{u} \cdot \nabla \mathbf{u})], \quad (11)$$

which implies that the square of the vorticity of the flow $\omega^2 = \text{tr}(\nabla \mathbf{u})^2$ is larger than the square of the strain rate $S^2 = \text{tr}(\nabla \mathbf{u} \cdot \nabla \mathbf{u})$. Fig. 10 shows the presence of connected regions of positive Q-criterion over the parts of the cube surface which correspond to the regions of increased heat transfer identified above. This supports the conclusion that the increased heat flux in these regions is caused by a vortex structure being generated by the 3D expansions around the cube corner.

The experimental results in Ref. [15] showed that beyond a certain Reynolds number (between 148×10^3 and 549×10^3), the strong expansion around the windward edges of a cube can cause a breakaway or shoulder separation to form. This behaviour has also been observed in hypersonic flows around cylinders [9] and 2D shapes [12]. Due to the orientation of the model in these experiments, the schlieren images (Fig. 11) do not capture the density variations (such as separation and re-attachment shocks) associated with such a separation. However, profiles of skin friction coefficient $C_f = 2\tau/\rho u^2$ obtained from the CFD simulations along the geometrical centreline of the cube (Fig. 12) show that C_f never drops below zero along the side faces of the cube. The CFD results therefore do not predict separation occurring even with the addition of incidence.

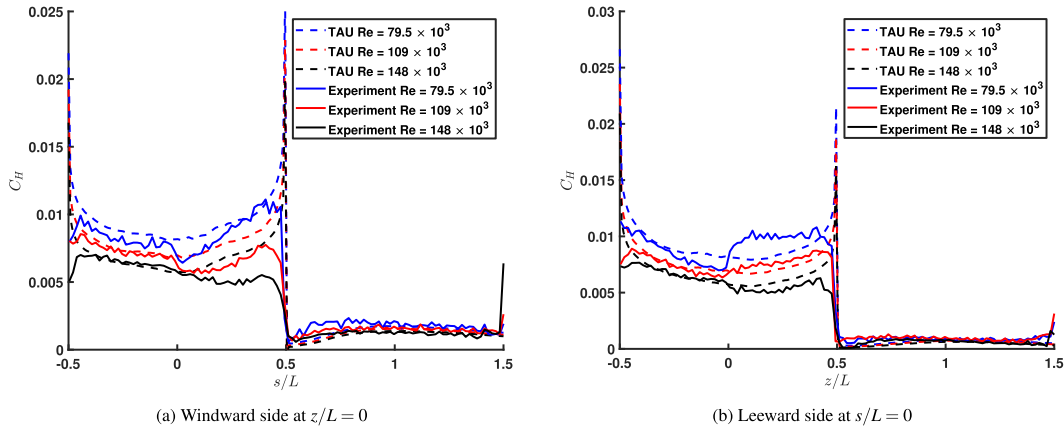
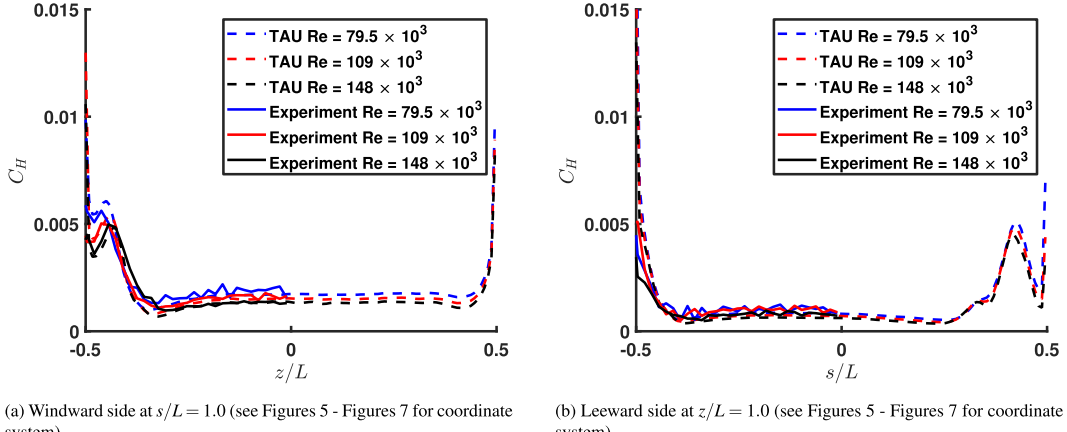
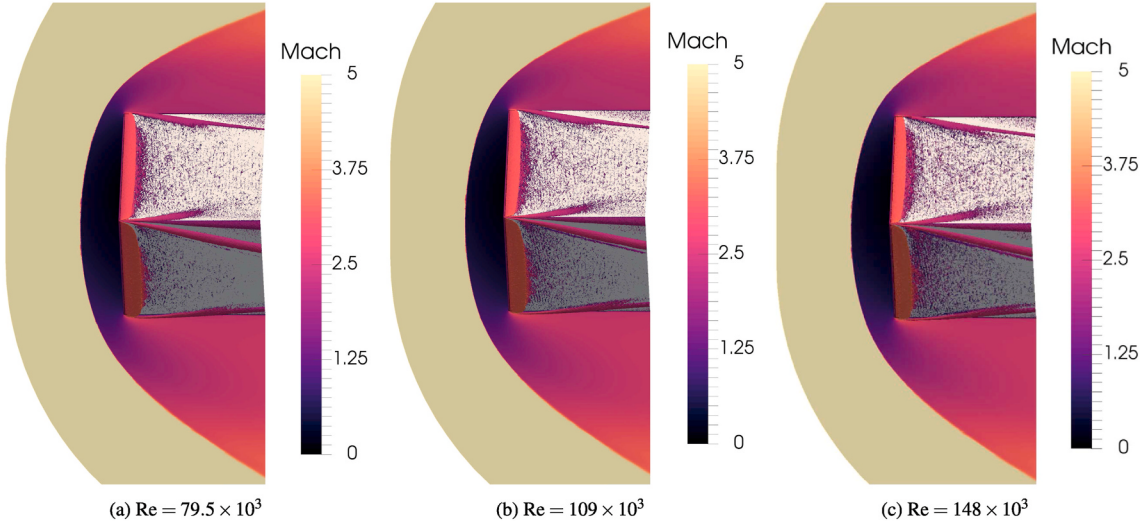
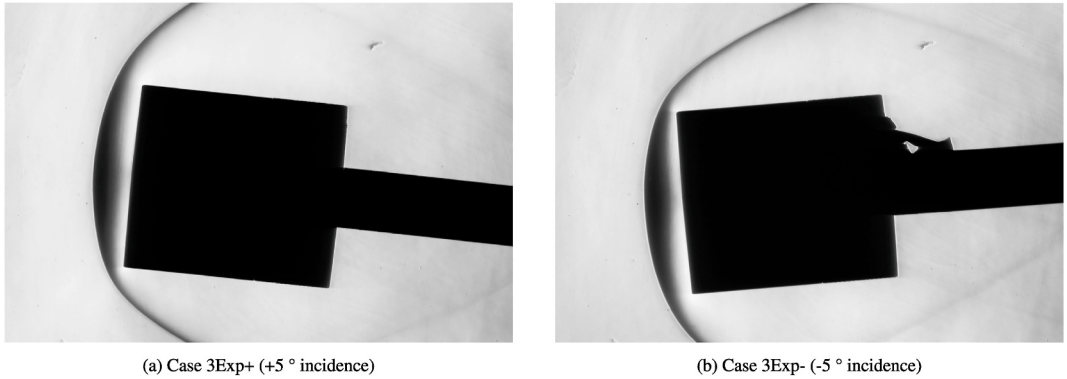


Fig. 8. Comparisons of experimental and numerical Stanton number along the geometrical centrelines of a cube at 5° incidence, in a Mach 5 flow and at a range of Reynolds numbers. Note that at each Reynolds number condition, the experimental data combines results from two different experiments.

(a) Windward side at $s/L = 1.0$ (see Figures 5 - Figures 7 for coordinate system).(b) Leeward side at $z/L = 1.0$ (see Figures 5 - Figures 7 for coordinate system).**Fig. 9.** Comparisons of experimental and numerical Stanton number on the off-stagnation surfaces of a cube at 5° incidence, in a Mach 5 flow and at a range of Reynolds numbers.**Fig. 10.** Figures showing CFD contours of Mach number and isosurfaces of normalized Q-Criterion around a cube at 5° incidence in a $M = 5$ flow and at a range of Reynolds numbers.**Fig. 11.** Schlieren images of a cube in a flow at $M = 5$ and $Re = 148 \times 10^3$ at $\pm 5^\circ$ incidence.

5. Discussion

5.1. Differences between CFD and experiment

The most significant differences between the experimental and numerical results occur at the sharp edges of the cube, where the numerical

results show very large spikes in heat flux which are not present in the experimental results. The apparent discontinuous nature of these heat flux increases makes it difficult to judge to what extent they are a physical phenomenon and to what extent they are simply a numerical artefact. In other words, although an increase in heat flux is expected to occur at the edge of the geometry due to the thinning of the boundary

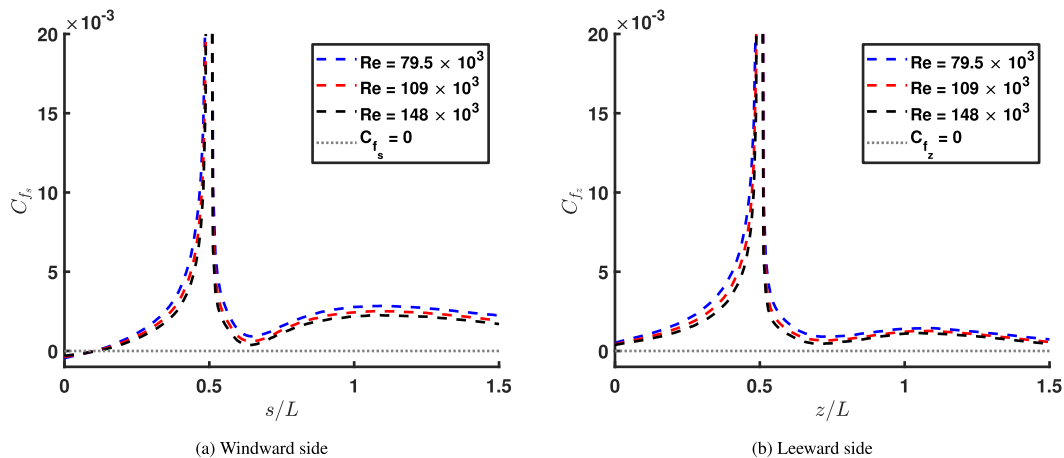


Fig. 12. Friction coefficient profiles along the geometrical centreline (leeward surface) of cubes at 5° incidence, in a Mach 5 flow and at three different Reynolds numbers.

layer through the flow expansion, the sheer size of the heat flux increase predicted by the numerical code seems un-physical. Furthermore, the magnitude of these spikes in heat flux could be amplified by the non-physicality of the boundary conditions used in the CFD solution, as discussed in Section 2.1. For the experimental case, an initial high heat flux would cause a large temperature increase in these regions. Consequently, increased rates of internal conduction in these regions could significantly change the wall temperatures and therefore heat fluxes in these regions. Such effects would be captured in the experimental results, but not in the numerical simulations. On the other hand, the extremely high temperatures seen at the edges and corners of the cube during the experiments may cause errors in the IRT temperature measurements. The calibration used for these experiments only extends to temperatures of $T = 676.5$ K, while the temperatures at the corners can increase beyond these values, especially near the end of the tunnel run (Fig. 4). Furthermore, as discussed in Section 3.1.2, the variation of Macor emissivity with temperature is unknown, and the very high temperatures experienced in these regions could significantly affect the accuracy of the temperature measurements made with the IR camera. These effects could be masking the amplitude of the heat flux increase at the edges and corners of the experimental results.

Another difference between the experimental and numerical results can be seen on the stagnation surface of the cube. In this region, the numerical results show a fairly smooth variation of heat flux, while the experimental results show significant noise and variation. Increased noise in the heat flux values on a planar hypersonic stagnation surface has been previously observed in the experiments of Laganelli [14]. The cause of these variations is unknown, and more detailed study of the flow in this region is warranted to fully understand this behaviour. In any case, this uncertainty in the experimental measurements on the stagnation surface of the cube makes it difficult to establish a single point which could be defined as a ‘stagnation point’. This would usually be the location on the stagnation surface with the lowest heat flux as the heat flux on the stagnation surface of a faceted surface actually increases as one moves away from the stagnation point. However, previous experiments of a cube at zero incidence in the HSST [15] suggested that the stagnation point could lie off-centre of the stagnation surface. In the previous study, this was attributed to flexing of the model mounting sting under aerodynamic load, leading to a slight misalignment of the cube to the oncoming flow. With the cube at incidence, the current experimental set-up was expected to induce a significant transverse load on the sting, which may lead to a displacement of the sting during the tunnel run. However, measurement of the displacement of the cube between wind-on and wind-off schlieren images showed that the sting flex in the vertical direction only increases the incidence of the cube by

about 0.1° for cases 3Exp+ and 3Exp- (the highest dynamic pressure free-stream conditions). This small change in incidence suggests that the noise in the heat flux measurements on the stagnation surface has a cause other than sting misalignment.

Away from the stagnation surface, another disagreement between the experimental and numerical heat flux results occurs immediately downstream of the expansion corner: $0.5 < s/L < 1$ on the windward side and $0.5 < z/L < 1$ on the leeward side (Fig. 8). In these regions, the experimental data shows consistently higher values of Stanton number compared to the numerical data. It is difficult to identify if this discrepancy is caused by an error in the CFD or experimental results (or both). As the boundary-layer passes around the expansion corner it undergoes an extremely strong expansion followed by a re-compression [15,43]. This is a region of the flow where viscosity is important and as a result, different viscous flux schemes used in the CFD solver could affect the numerical results in this region. At the same time, this is a region in the experimental results where sensitivity to the edge detection in the image processing algorithm is especially important. Nevertheless, both sets of results show the same physically correct trends: the Stanton number values are inversely proportional to Reynolds number.

We also note that earlier studies [9] of the hypersonic heat fluxes in the region immediately downstream of a strong expansion corner found it very challenging to measure the heat flux in this region, possibly due to the extreme sensitivity of the flow in this region to the Reynolds number. When considering the flow in this region, and indeed all of the side faces of the cube, it is worth recalling that the CFD simulations are laminar Navier-Stokes solutions – no turbulence model is used. This assumption was justified in Section 2.1 due to the relatively low Reynolds numbers of the flow and the fact that the heat flux agreement for $z/L > 1.0$ and $s/L > 1.0$ is better than $0.5 < s/L < 1$ and $0.5 < z/L < 1$ supports the idea that this is not a turbulent flow effect. The fact that we see such good agreement on the side surfaces of the cube, and especially within the vortex-induced hot wedges (for example, in Fig. 9) further supports the assumption of laminar flow in the CFD simulations.

5.2. The effect of incidence on the hypersonic flow around a cube

When compared to the heat fluxes measured on a cube at 0° incidence, the most obvious effect of the addition of incidence is the different behaviour of the vortex structures generated by the 3D expansions around the windward corners of the cube. No vortices form at the outer edges of the cube on the windward half, while the vortices on the leeward half are larger. This is most likely due to the negative pressure gradient from the windward to the leeward halves of the cube. In this sense, we propose that these vortices can be thought of as anal-

ogous to wingtip vortices of aircraft, or leading edge vortices on highly swept wings. A consequence of the presence of these vortices is that the aerodynamic coefficients of the cube may differ from those predicted by methods such as modified Newtonian impact theory (as vorticity could change the effective angle of attack of the geometry). To investigate this phenomenon, the aerodynamic lift and drag coefficients of the cube were estimated by integrating the distributions of C_p and C_f over the cube's surface, as predicted by the CFD simulations. For these calculations it was assumed that $C_p = C_f = 0$ on the back surface of the cube (this region was not modelled by the CFD). Values of C_D and C_L , as well as L/D for each of the flow conditions are presented in Table 5. These results show little to no dependence on Reynolds number. For comparison, modified Newtonian impact theory gives values of $C_D = 1.4$, $C_L = 0.0076$, and $L/D = 0.0054$. The significant differences between the modified Newtonian and CFD values of C_L are likely due to the large suction regions on the leeward half of the cube where $C_p < 0$. This effect cannot be captured by modified Newtonian theory.

The effect of incidence on the stagnation point heat flux is less evident. In 1964 Klett [8] studied the stagnation point heat flux behaviour to discs (which we consider an equivalent planar surface to the stagnation surface of the cuboid) normal to an oncoming hypersonic free-stream. The results of Klett's study suggested that the stagnation point heat flux changes negligibly as the incidence is increased up to 30° , at which point the stagnation point heat flux starts to increase significantly with increasing incidence, reaching a maximum at 45° (when the stagnation point essentially lies on the edge of the disc) before decreasing again as the incidence is further increased to 90° . We therefore might expect the stagnation point heat fluxes of the current results to be very similar to the results reported in Ref. [15] (which considered a cube at 0° incidence). In fact, the current numerical heat fluxes are on average 5% higher than the earlier experimental results which is within the experimental error bounds.

5.3. In the context of satellite Re-Entry heating models

Obviously, performing detailed CFD simulations and experiments for every satellite re-entry risk analysis is not feasible. Instead, demise analysis tools must make use of correlations of data generated by these high fidelity methods. One common way of correlating heat fluxes to simple shapes such as cuboids is through the use of a heating shape factor, F_{sh} , defined as:

$$F_{sh} = \frac{\hat{q}}{q_{ss}} \quad (12)$$

where \hat{q} is the space-averaged heat flux to the object:

$$\hat{q} = \frac{\int_S q dS}{S} \quad (13)$$

and q_{ss} is the stagnation point heat flux to a sphere with radius equivalent to the effective nose radius of the object being considered. For a cuboid geometry such as the one considered in this study, the effective nose radius $R_n = L/2$. Satellite demise analysis tools such as DRAMA [4] have a library of shape factors for different primitive shapes such as cubes, cylinders, and hemispheres at a range of different orientations to the free-stream flow. They then calculate q_{ss} using a simple correlation for stagnation point heat flux to a sphere (for example, using the Sutton & Graves [44] or Fay & Riddell [45] correlations) and multiply the result by the appropriate shape factor to get the average heat flux to the object under consideration. This is an extremely quick and efficient manner of estimating the variation of the heat load to a geometry as it undergoes atmospheric re-entry. Due to the fact that the current experimental dataset does not contain Stanton numbers for the flow over the entire cube, it is not possible to calculate experimental shape factors using the present experimental data. Shape factors for the CFD data are presented in Table 5. In general, due to the broad agreement between the CFD and

experimental data, we expect these CFD values to be representative of the true values, with the caveat that we would expect the numerical shape factors to be slightly higher than the equivalent experimental values. This is because of the large spikes in heat flux near the edges and corners of the cube which are present in the numerical (but not experimental) data.

Although the shape factor heating model described above is extremely computationally efficient, it still only represents an average heating rate, and cannot capture the significant spatial variations in heat flux experienced by faceted shapes. This is important because the highest heat fluxes for faceted shapes are expected to occur near the corners and edges of the geometry. Furthermore in the case of a satellite these regions are often the locations of the epoxy-potted-joints which fasten the honeycomb sandwich panels together [46] (illustrated in Fig. 13). The epoxy which bonds these joints together could fail before any melting or ablation of the satellite structure occurs. Therefore understanding the temperature evolution of these joints may be key to understanding the fragmentation and demise of a satellite during re-entry [47].

To take these spatial variations of heat flux near the sharp corners and edges into account, a previous study of the hypersonic heat fluxes to cubes [15] proposed using edge-specific shape factors to model the heating experienced by a faceted shape during re-entry. By this definition, only certain edges of the cube are used to calculate the average in Equation (13). Depending on the fidelity of the simulation required, edges can be further separated into three categories: windward, streamwise, and leeward. The definition of an 'edge' is specific to the application, but in general it can be defined as the region of the geometry surface within some distance x of the spatial discontinuity (or sharp corner). The exact value of x is then application specific. For example, if it is known that the epoxy joints holding the satellite panel together have a length of δ then $x = \delta$ would be the most appropriate value to use. The edge specific heating shape factors for the current results, calculated using the numerical results are presented in Fig. 14. This plot shows that there is very little Reynolds number variation for the all-edges and windward-edges shape factors. However, likely due to the viscous nature of the vortex structures along the streamwise edges of the cube, the streamwise-edges shape factor shows a small increase with Reynolds number. Overall, compared to the results presented in Ref. [15] there is very little difference between the shape factors of a cube at 0° (Table 5) and 5° incidence (Table 4). If anything, the addition of incidence reduces the shape factors slightly.

6. Conclusions

Previous experimental studies of the hypersonic flow around cuboid geometries [13–15] have only focused on taking measurements of models at zero incidence to the free-stream flow. In order to build a complete understanding of the heat fluxes experienced by faceted shapes during atmospheric re-entry events, it is necessary to examine how these values change as the object tumbles (that is, when its attitude changes) during the re-entry trajectory. This work has studied the Mach 5 flow around a cube at 5° incidence using both experimental and numerical methods. Experimental heat flux measurements were taken using infrared thermography and an IHCP data reduction method, and the experimental flowfield was visualized using schlieren photography. The CFD results complementing these experimental results were obtained using the DLR-TAU code.

There was good agreement between the Stanton number contours generated by the CFD simulation and the experimental results. These heat flux results showed the presence of wedge-shaped regions of increased heat flux along the streamwise edges of the cube, which emanated from the sharp windward corners of the cube. It has previously been suggested that these regions of high heat flux are generated by the strong 3-dimensional expansion around the windward corners of the cube [15]. Visualization of numerical Q-criterion isosurfaces has

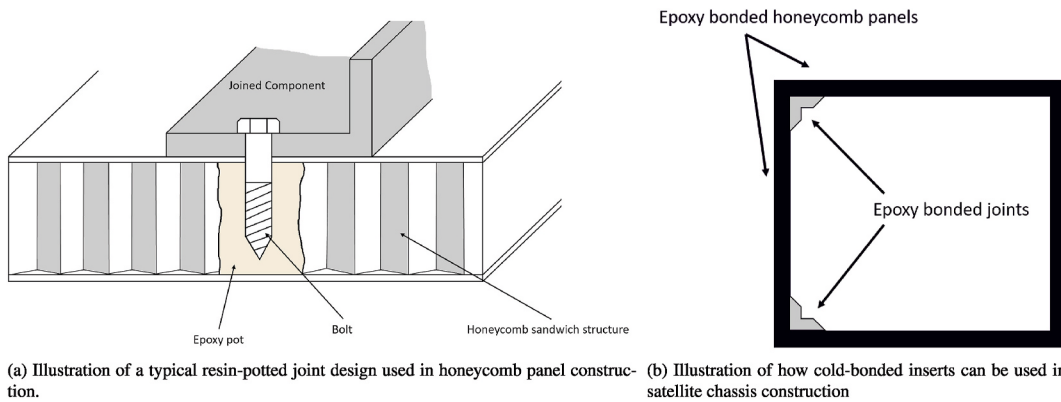


Fig. 13. Satellite construction using epoxy-potted joints.

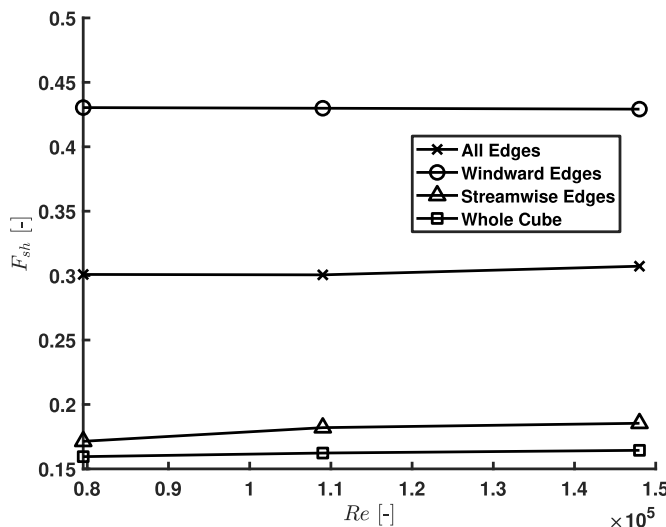
Fig. 14. Dependence of various shape factor definitions on Reynolds number for a cube at 5° incidence at $M = 5$.

Table 4

Summary of key experimental heating results from Ref. [15] for a cube at 0° incidence at $M = 5$.

$Re \times 10^3$	$C_{H_0} \times 10^{-3}$	F_{sh}
79.5	8.1	0.1679
109	6.4	0.1611
148	5.7	0.1612

Table 5

Key results from the current CFD simulations for a cube at 5° incidence at $M = 5$.

Case No.	$Re \times 10^3$	C_D	C_L	L/D	$C_{H_0} \times 10^{-3}$	F_{sh}
1	79.5	1.623	0.0620	0.0382	8.5	0.1595
2	109	1.621	0.0624	0.0385	7.2	0.1623
3	148	1.620	0.0623	0.0385	6.1	0.1644

confirmed that vortex structures are present near these regions of increased heat flux. When compared to experiments on a cube at 0° incidence, the shapes of these vortex structures show a strong dependence on incidence. Notably, no vortices form at the outer edges of the cube on the windward side, while the vortices on the leeward side are larger.

Compared to previous studies of the heat fluxes experienced by cubes

at 0° incidence, the stagnation point heat flux values are not significantly affected by the addition of incidence to the geometry. This behaviour is consistent with previous studies of flow to planar stagnation points, notably the work by Klett [8] on discs. Similarly, the average heating to the cube, represented by the heating shape factor F_{sh} , shows only a very weak dependence on incidence. In addition to the whole-cube shape factor, other edge-specific shape factors were calculated with the CFD results. These shape factors represent the average heating to the edges of the cube and therefore can capture the variation of most important regions of heating over the cube's surface. In contrast to the whole-cube shape factor, the edge-specific values (especially the streamwise-edge shape factor) showed a positive correlation with Reynolds number.

Declaration of competing interest

The authors declare that they have no known competing financial interests or personal relationships that could have appeared to influence the work reported in this paper.

Acknowledgments

TWR would like to acknowledge the financial and technical support of the European Space Agency (under NPI 480-2015), Fluid Gravity Engineering, and the Engineering and Physical Sciences Research Council UK through the Imperial College London Centre for Doctoral Training in Fluid Dynamics Across Scales (grant EP/L016230/1). The experimental work presented here was further supported financially by the award of a UK Fluids Network Short Research Visit grant. The authors would also like to thank the workshop at the Imperial College London Department of Aeronautics for manufacturing the models used in the experiments, and Jeroen Van den Eynde and Csaba Jeger at ESA-ESTEC for their help with TAU.

References

- [1] D.J. Kessler, B.G. Cour-Palais, Collision frequency of artificial satellites: the creation of a debris belt, *J. Geophys. Res.* 83 (1978) 2637–2646.
- [2] IADC, Inter-Agency Space Debris Coordination Committee, Space Debris Mitigation Guidelines, Technical Report 22, Inter-Agency Space Debris Coordination Committee, 2007, http://www.iadc-online.org/Documents/IADC-2002-01_IADCSpaceDebrisGuidelines,Revision1.pdf.
- [3] R. Reynolds, P. Eichler, An overview of revised NASA safety standard 1740.14, in: Second European Conference on Space Debris, Darmstadt, Germany, 1997, pp. 721–726.
- [4] C. Martin, J. Cheese, N. Sanchez Ortiz, K. Bunte, H. Klinkrad, T. Lips, B. Fritzsche, G. Koppenwallner, DRAMA 2.0 Final Report, European Space Agency, 2005. Technical Report.
- [5] G. Koppenwallner, B. Fritzsche, T. Lips, H. Klinkrad, SCARAB - a multidisciplinary code for destruction analysis of space-craft during re-entry, in: Proceedings of the Fifth European Symposium on Aerothermodynamics for Space Vehicles, Cologne, Germany, 2005.

- [6] J. Dobarco-Otero, R.N. Smith, K.J. Bledsoe, R.M. Delaune, W.C. Rochelle, N. L. Johnson, The Object reentry survival analysis tool (Orsat) version 6.0 and its application to spacecraft entry, in: 56th International Astronautical Congress of the International Astronautical Federation, the International Academy of Astronautics, and the International Institute of Space Law, Fukuoka, Japan, 2005.
- [7] D.M. Kuehn, Experimental and Theoretical Pressures on Blunt Cylinders for Equilibrium and Nonequilibrium Air at Hypersonic Speeds, Technical Report, Ames Research Center, NASA TN D-1979, Moffett Field, CA, 1963.
- [8] R.D. Klett, Drag Coefficients and Heating Ratios for Right Circular Cylinders in Free-Molecular and Continuum Flow from Mach 10 to 30, Sandia National Laboratory, Albuquerque, NM, 1964. Technical Report.
- [9] R.K. Matthews, R.H. Eaves Jr., Comparison of Theoretical and Experimental Pressure and Heat Transfer Distributions on Three Blunt Nosed Cylinders in Hypersonic Flow, Technical Report, Arnold Engineering Development Center, AEDC-TR-67-148, Arnold Air Force Station, TN, 1967.
- [10] M. Inouye, J.G. Marvin, A.R. Sinclair, Comparison of Experimental and Theoretical Shock Shapes and Pressure Distribution on Flat-Faced Cylinders at Mach 10.5, Technical Report, Ames Research Center, NASA TN D-4397, Moffett Field, CA, 1968.
- [11] R.H. Eaves Jr., An Empirical Correlation of Pressure on Blunt-Nosed Cylindrical After bodies at Hypersonic Mach Numbers, Technical Report, Arnold Engineering Development Center, AEDC-TR-68-82, Arnold Air Force Station, TN, 1968.
- [12] T.W. Rees, P. Bruce, J.A. Merrifield, The effect of Reynolds number on the hypersonic flow around faceted shapes, in: 22nd AIAA International Space Planes and Hypersonics Systems and Technologies Conference, Orlando, FL, 2018, <https://doi.org/10.2514/6.2018-5197>.
- [13] E.C. Crosby, W.A. Knox, Heat Transfer and Static Stability Tests of the General Purpose Heat Source (GPHS) Configurations at Mach 8.0. Technical Report, AEDC-TSR-80-V7, Technical Report, AEDC-TSR-80-V7, Arnold Air Force Station, TN, 1980.
- [14] A.L. Lagannelli, Analytical and Experimental Heat Transfer and Flow-Field Prediction on a Rectangular Reentry Module, Technical Report, SAI-067-81R-001, Science Applications inc., Wayne, PA, 1980.
- [15] T.W. Rees, T.B. Fisher, P.J.K. Bruce, J.A. Merrifield, M.K. Quinn, Experimental characterization of the hypersonic flow around a cube, *Exp. Fluid* 61 (2020).
- [16] S.X. Li, Y.K. Chen, Z.Y. Ni, Flowfield features on hypersonic flow over rectangular obstacles, *J. Visual* 4 (2001) 73–79.
- [17] Y. Prévereaud, J.-I. Vérant, J. Annaloro, S. Galera, Development of new analytical models of pressure and heat transfer distributions on space debris uncontrolled atmospheric entry : planar bodies, in: Proceedings of the 7th European Conference for Aerodynamics and Space Sciences, EUCASS, 2017, p. 5959.
- [18] J. Annaloro, S. Galera, C. Thiebaut, M. Spel, P. van Hauwaert, G. Grossir, S. Paris, O. Chazot, P. Omaly, Aerothermodynamics modelling of complex shapes in the Debris atmospheric reentry tool: methodology and validation, *Acta Astronaut.* 171 (2020) 388–402.
- [19] M. Spel, V. Rivola, B. Plazolles, First spacecraft demise workshop-Test case description and results, in: 8th European Symposium on Aerothermodynamics for Space Vehicles, Portugal, Lisbon, 2015. <https://hal.laas.fr/hal-02175370>.
- [20] J. Van Den Eynde, L. Ferracina, G. Prigent, Activities of the AeroThermoDynamics and design for demise (ATD3) working group, in: 4th International Workshop on Space Debris Re-entry, Darmstadt, Germany, 2018.
- [21] J. Van Den Eynde, S. Lemmens, CFD computations of orbital and super-orbital Re-entry heating on primitive shapes, in: 1st International Conference on Flight Vehicles, Aerothermodynamics, and Re-entry Missions and Engineering, Monopoli, Italy, 2019.
- [22] D. Schwamborn, T. Gerhold, R. Heinrich, The DLR TAU-code: recent applications in research and industry, *ECCOMAS CFD* (2006) 1–25.
- [23] D.E. Boutamine, P. Reynier, R. Schmehl, L. Marraffa, J. Steelant, Computational analysis of automated transfer vehicle reentry flow and explosion assessment, *J. Spacecraft Rockets* 44 (2007) 860–870.
- [24] A. Gülnan, D. Neeb, T. Thiele, F. Siebe, Aerothermal postflight analysis of the sharp edge flight experiment-II, *J. Spacecraft Rockets* 53 (2016) 153–177.
- [25] M.S. Liou, Ten years in the making – AUSM-family, in: 15th AIAA Computational Fluid Dynamics Conference, Anaheim, CA, 2001.
- [26] F. McNeil Cheatwood, P.A. Gnoffo, User's Manual for the Langley Aerothermodynamic Upwind Relaxation Algorithm (LAURA), Technical Report, NASA Langley Research Center, Hampton, Va., 1996.
- [27] P. Papadopoulos, E. Venkatapathy, D. Prabhu, M.P. Loomis, D. Olynick, Current grid-generation strategies and future requirements in hypersonic vehicle design, analysis and testing, *Appl. Math. Model.* 23 (1999) 705–735.
- [28] E. Erdem, Active Flow Control Studies at Mach 5: Measurement and Computation, Doctoral thesis, University of Manchester, 2011.
- [29] T.B. Fisher, Development of Advanced Techniques for Aerodynamic Assessment of Blunt Bodies in Hypersonic Flows, Doctoral thesis, University of Manchester, 2019.
- [30] G. Cardone, A. Ianiero, G. Dello Ilio, A. Passaro, Temperature maps measurements on 3D surfaces with infrared thermography, *Exp. Fluid* 52 (2012) 375–385.
- [31] M. Imbriale, Inverse Heat Transfer Method for Ceramic Materials Thermo-Physical Properties Evaluation, Doctoral, University of Naples Federico II & EMASpa, 2013.
- [32] W.A. Clayton, A 500 to 4500 F thermal radiation test facility for transparent materials, in: J.C. Richmond (Ed.), Measurement of Thermal Radiation Properties of Solids, Dayton, OH, 1962.
- [33] Rigur Polyjet Simulated Polypropylene Material Data Sheet, 2016.
- [34] G.M. Carlomagno, G. Cardone, Infrared thermography for convective heat transfer measurements, *Exp. Fluid* 49 (2010) 1187–1218.
- [35] M. Zaccara, S. Cerasuolo, G. Cardone, J.B. Edelman, S.P. Schneider, Infrared thermography data reduction technique for heat transfer measurements in the Boeing/AFOSR Mach-6 quiet tunnel, in: AIAA Scitech 2019 Forum, January, 2019, pp. 1–14, <https://doi.org/10.2514/6.2019-0894>.
- [36] S. Rajagopalan, R.A. Robb, Image smoothing with Savitzky-Golay filters, *Medical Imaging 2003: Visualization, Image-Guided Procedures, and Display* 5029 (2003) 773.
- [37] H.S. Ying, Savitzky-Golay Smoothing Filter for 3D Data, 2020. <https://uk.mathworks.com/matlabcentral/fileexchange/37148-savitzky-golay-smoothing-filter-for-3d-data>.
- [38] M. Guizar-Sicairos, S.T. Thurman, J.R. Fienup, Efficient subpixel image registration algorithms, *Optic Lett.* 33 (2008) 156–158.
- [39] M.N. Ozisik, H.R.B. Orlande, Inverse Heat Transfer Fundamentals and Applications, first ed., Taylor and Francis, 2000.
- [40] C.H. Huang, S.P. Wang, A three-dimensional inverse heat conduction problem in estimating surface heat flux by conjugate gradient method, *Int. J. Heat Mass Tran.* 42 (1999) 3387–3403.
- [41] C.R. Martin, HOT Thermodynamic Tools for Matlab, 2019. <https://www.mathworks.com/matlabcentral/fileexchange/26430-hot-thermodynamic-tools-for-matlab>.
- [42] J.C.R. Hunt, A.A. Wray, P. Moin, Eddies, streams, and convergence zones in turbulent flows, in: Center for Turbulence Research, *Proceedings of the Summer Program*, 1970, 1988, pp. 193–208.
- [43] L.G. Kaufman II, L. Meckler, S.A. Hartofilis, An investigation of flow separation and aerodynamic controls at hypersonic speeds, *J. Aircraft* 3 (1966) 555–561.
- [44] K. Sutton, R.A. Graves Jr., A General Stagnation-Point Convective-Heating Equation for Arbitrary Gas Mixtures, NASA TR R-376, Technical Report, NASA Langley Research Center, Hampton, Va., 1971.
- [45] J.A. Fay, F.R. Riddell, Theory of stagnation point heat transfer in dissociated air, *J. Aero. Sci.* 25 (1958) 73–85.
- [46] G. Bianchi, Structural Performance of Spacecraft Honeycomb Panels, Engd thesis, University of Southampton, 2011.
- [47] T. Soares, J.A. Merrifield, Characterization of tests of structural joints behaviour during Re-entry, in: 4th International Workshop on Space Debris Re-entry, ESOC, Darmstadt, Germany, 2018.